NJC

ROYAL SOCIETY OF CHEMISTRY

PAPER

View Article Online
View Journal | View Issue

Cite this: *New J. Chem.*, 2023, **47**, 4206

Hexagonal cobalt oxide nanosheet-based enzymeless electrochemical uric acid sensor with improved sensitivity

Vandana Nagal,†[a] Marya Khan,†[b] Sakeena Masrat,[b] Shamshad Alam,[c] Akil Ahmad,[d] Mohammed B. Alshammari,[d] Kiesar Sideeq Bhat[ef] and Rafiq Ahmad *[b]

Enzymeless sensors have been known as highly stable, fast, and reliable devices for the detection of several biomolecules and for use in early disease diagnosis. Hence, it is crucial to fabricate enzymeless sensors with high sensitivity. Herein, we describe the synthesis of hexagonal cobalt oxide nanosheets using a hydrothermal method. The crystalline phase of the as-synthesised cobalt oxide nanosheets was examined using X-ray diffraction (XRD), and the morphology was observed using field emission scanning electron microscopy (FESEM) and transmission electron microscopy (TEM). The cobalt oxide nanomaterials were synthesised in a large quantity and showed a uniform and hexagonal nanosheet like morphology. To investigate their application, the nanosheet nanomaterial was utilised to fabricate an ultra-sensitive enzymeless electrochemical-based uric acid (UA) sensor on a screen-printed carbon electrode (SPCE). A paste of hexagonal cobalt oxide nanosheets in a conductive binder was drop-casted onto the working electrode of the SPCE. The cobalt oxide nanosheet-based UA sensor showed a good response for UA detection. Under optimal conditions, the cobalt oxide/SPCE UA sensor showed linearity up to 200 μM of UA with ultra-sensitivity (1560 μA mM^{-1} cm^{-2}) and a limit of detection of ~5 μM. Furthermore, the fabricated UA sensor was subjected to reproducibility, storage stability, and selectivity tests, which confirmed good stability, reproducibility, and specificity for UA. The developed ultra-sensitive enzymeless UA sensor is expected to be useful for the sensing of UA in real samples.

Received 28th December 2022,
Accepted 23rd January 2023

DOI: 10.1039/d2nj06331j

rsc.li/njc

1. Introduction

Uric acid (UA) is a "natural waste product" that is produced during digestion of foods that contain purines, and it is eliminated from the body in urine and faeces.[1] However, the UA accumulates in the body when too much is produced or the body fails to excrete it. High UA levels affect the kidneys and the lower extremities.[2] Abnormal levels of UA cause lethal effects in the human body, such as gout, fatty liver, renal diseases, kidney stones, hypertension, cardiovascular disease, obesity, diabetes, and metabolic syndrome. Hence, it is essential to routinely screen the UA levels for the occurrence of the disease which then enables timely treatment. There are several methods, *i.e.*, high-performance liquid chromatography, chemiluminescence, mass spectrometry, colorimetry, capillary electrophoresis-amperometry, spectrophotometry, ion chromatography, electrochemical-based sensors, and enzymatic test-kits, which are utilised to detect the level of UA.[3–7] However, the majority of these diagnostic methods are complex, take time to perform, and are expensive.[8]

Recently, more attention has been paid to electrochemical-based UA sensors due to their excellent sensitivity, simple fabrication procedure, short response time, ease of handling, and good selectivity.[9–12] However, most of the electrochemical-based UA sensors have been fabricated using enzymes.[9–12] The enzyme-based sensors are not suited for large scale fabrication because they require a controlled environment for their storage. Also, the high cost of enzymes, utilisation of complex enzyme immobilisation methods, and sensitive nature of the enzymes

[a] *Quantum and Nanophotonics Research Laboratory, Centre for Nanoscience and Nanotechnology, Jamia Millia Islamia, New Delhi, 110025, India*
[b] *Sensors Lab, Centre for Nanoscience and Nanotechnology, Jamia Millia Islamia, New Delhi, 110025, India. E-mail: rahmad5@jmi.ac.in*
[c] *Department of Pharmacology & Therapeutics, Rosewell Park Comprehensive Cancer Institute, Buffalo, NY, 14263, USA*
[d] *Department of Chemistry, College of Science and Humanities in Al-Kharj, Prince Sattam Bin Abdulaziz University, Al-Kharj-11942, Saudi Arabia*
[e] *Singapore-MIT Alliance for Research and Technology (SMART), Critical Analytics for Manufacturing of Personalized-Medicine (CAMP), Singapore, 138602, Singapore*
[f] *Department of Bioresources, University of Kashmir, Hazratbal, Srinagar, 190006, India*
† Authors contributed equally to this work.

are other critical factors. To avoid the complexity of the enzyme-based sensors, researchers nowadays are working more with enzymeless sensors in which nanomaterial-based sensors are used more as they are low-cost, and have enhanced sensitivity, and reduced complexity.[13–15]

Recently, different nanostructured materials (*i.e.*, CeO_2, Co_3O_4, CuO, Cu_2O, Fe_2O_3, MgO, MnO_2, MoS_2, NiO, SnO_2, and ZnO) have been used to fabricate electrochemical-based enzymeless UA sensors.[16–19] Among these nanomaterials, cobalt oxide has gained interest as an superior electrochemical material for electrodes and offers excellent catalytic properties.[20] Various morphologies of the cobalt oxide have been synthesised using chemical vapour deposition, sol–gel techniques, chemical precursor routes, and electrophoretic deposition techniques.[21] The synthesised nanostructures of cobalt oxide are frequently used for electrochemical sensing, energy storage, and energy conversion applications due to their fast electron communication and good catalytic properties.[22–26] Cobalt oxide nanostructures are preferred for modifying the working electrode of enzymeless sensors because of their high electrochemical activity and good electrical performance.[27]

In this work, we report the successful synthesis of hexagonal cobalt oxide nanosheets by a simple and reproducible hydrothermal method. The as-synthesised nanomaterial was examined using XRD, FESEM, and high-resolution TEM (HR-TEM) techniques to elucidate the morphology and crystallinity. The hexagonal cobalt oxide nanosheets were utilised to fabricate an electrochemical-based enzymeless UA sensor. A paste of conductive binder and hexagonal cobalt oxide nanosheets was fixed onto the working electrode of the SPCE during sensor fabrication. The cobalt oxide nanosheets/SPCE exhibited excellent catalytic activity for UA with a high sensitivity and a low limit of detection (LOD). In addition, other tests, *i.e.*, storage stability, fabrication reproducibility, and selectivity were also performed. This work demonstrates the use of cobalt oxide nanosheets for fabricating an enzymeless UA sensor, which could also be applied in the design of energy related and other highly efficient medical devices.

2. Experimental details

2.1. Chemicals

All analytical chemicals were utilised as-received without any additional refinement. Cobalt nitrate hexahydrate ($Co(NO_3)_2 \cdot 6H_2O$; ≥99.99%), NaOH pellets (97%), ethanol (laboratory reagent), potassium chloride (KCl; 99.0–100.5%), sodium chloride (NaCl), potassium hexacyanoferrate(III) $(K_3Fe(CN)_6)^{3-/4-}$ (≥99.0%), glucose, fructose, urea, lactic acid (LA), L-cysteine, phosphate buffered saline (PBS) pellets, and conductive binder (ethylene glycol; 99.8%) were purchased from Sigma-Aldrich. The SPCE (length = 3 cm, width = 0.7 cm, and the gap between the electrodes = 0.35 cm) were purchased from PalmSens (The Netherlands).

2.2. Synthesis of hexagonal-shaped cobalt oxide nanosheets

The hexagonal-shaped cobalt oxide nanosheets were synthesised using a low temperature-based hydrothermal method.[28] In brief, 0.765 g (0.12 M) of $Co(NO_3)_2 \cdot 6H_2O$ precursor was added to 35 mL of distilled water and thoroughly mixed to obtain a homogeneous mixture. Then, 0.3 M NaOH was added drop-wise into the previous solution with stirring at 500 rpm until the pH of mixture reached to 13. Next, the homogeneous mixture was poured into a Teflon-lined stainless steel autoclave (100 mL capacity,) and heated at 180 °C for 6 h. Next, after cooling down the stainless-steel autoclave, the precipitate obtained was washed three times with distilled water and ethanol using centrifugation (5000 rpm for 10 min). The sample was poured into a glass Petri dish and kept for drying at 60 °C. Finally, the dried powder was annealed at 450 °C for 3 h. The schematic of synthesis process is shown in Fig. 1.

2.3. Fabrication of an ultra-sensitive enzymeless UA sensor

To fabricate the electrochemical-based enzymeless UA sensor, firstly, the as-synthesised hexagonal shaped cobalt oxide nanosheets (0.02 g) were mixed with 120 μL of conductive binder (ethylene glycol) using ultra-sonication (10 min) to obtain a nanomaterial slurry. Next, the as-prepared slurry was drop-casted (3 μL, 6 μL, or 9 μL) onto the SPCE (working electrode area) and dried at 30 °C. The fabricated enzymeless UA sensors (cobalt oxide nanosheets/SPCE) were stored at room temperature.

2.3. Characterizations

For the crystal structure determination, XRD was performed (CuKα radiation; λ = 1.5406 Å) using a diffractometer (Rigaku). The morphology of the nanostructure was observed using a Sigma FESEM (Zeiss) and a TECNAI G2 HR-TEM (ThermoScientific). The electrochemical characterisation of the fabricated sensor was done using a compact, portable, versatile, and powerful PalmSens4 potentiostat/impedance analyser (PalmSens). During the measurement, the surface modified SPCE was connected with an SPE connector. The sensor fabrication was optimised using an impedance analyser. The cyclic voltammetry (CV) response and impedance of each fabricated sensor was determined in 5 mM $[Fe(CN)_6]^{3-/4-}$ with a 0.1 M KCl probe solution (scan rate = 50 mV s^{-1}) and the best performing sensor was selected for

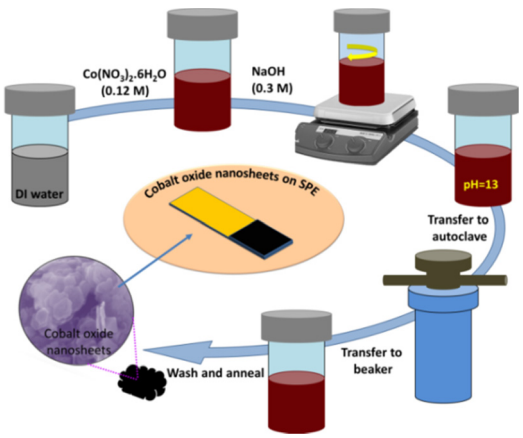

Fig. 1 A schematic illustration of the hexagonal shaped cobalt oxide nanosheet synthesis procedure using a hydrothermal method, and the UA sensor fabrication.

further analysis. All the CV measurements were done in PBS buffer with an optimised pH of 7.4.[29]

3. Results and discussion

3.1. Morphological and structural characterisation of the hexagonal cobalt oxide nanosheets

The morphology of the as-synthesised pristine cobalt oxide nanomaterial was investigated using FESEM. As shown in Fig. 2(a–c), the cobalt oxide nanostructures were synthesised in large quantity and showed a sheet-like morphology with uniform size distribution. A closer look at the high resolution FESEM image showed that the synthesised cobalt oxide nanosheets were hexagonal in shape. Fig. 2d shows the XRD pattern of the hexagonal shaped cobalt oxide nanosheets, which was similar to previously reported data.[30] All the observed diffraction peaks were well-matched with the JCPDS 42-1467 results. The XRD analysis confirmed the phase purity of the cobalt oxide nanosheets. The XRD peaks obtained at various angles corresponded to different planes: (111), (220), (311), (222), (400), (422), (511), and (440). Also, no other peak representing any impurity was observed. This suggested that the synthesised hexagonal shaped cobalt oxide nanosheets were of high purity.

Furthermore, for detailed analysis, TEM imaging of the cobalt oxide nanosheets was also performed (Fig. 3). Fig. 3(a–c) display the TEM images of the cobalt oxide nanosheets at different magnifications. These TEM images confirmed the thin and hexagonal shape of the cobalt oxide nanosheets. Fig. 3d shows the HR-TEM image with the selected-area electron diffraction (SAED; upper inset of Fig. 3d) and the magnified HR-TEM image (lower inset of Fig. 3d). This validated the crystalline nature of the cobalt oxide nanosheets and is consistent with XRD observations.

3.2. Electrochemical activity analysis

The electrochemical analysis of the electrodes (bare and modified) was performed using electrochemical impedance spectroscopy (EIS). The EIS was used to analyse the interfacial and electron transfer feature of the modified electrodes. We recorded the charge transfer resistance of the bare SPCE and the cobalt oxide nanosheet modified SPCE in probe electrolyte (5 mM $[Fe(CN)_6]^{3-/4-}$ and 0.1 M KCl). Fig. 4a displays the EIS Nyquist plots for the bare SPCE (a), and after modification with 3 μL (b), 6 μL (c), and 9 μL (d) cobalt oxide nanosheet slurry on SPCE. Notably, the charge transfer resistance value of the 6 μL cobalt oxide nanosheet modified SPCE was lower than that of the other bare and modified electrodes (Fig. 4b). Hence, the 6 μL cobalt oxide nanosheet is the appropriate amount to modify SPCE for achieving superior electrocatalytic and electron transfer properties. The probable reason for the high resistance for the 3 μL cobalt oxide modified electrode may be due to the insufficient amount of cobalt nanosheets to efficiently carry forward the fast current response. Whereas for the 9 μL cobalt oxide modified electrode it may be due to the excessive amount of cobalt nanosheets, *i.e.*, the film thickness on the active area, which eventually opposed the charge flow and thus, gave rise to more resistance. Moreover, it was clear that the 6 μL modified SPCE showed less resistance than the bare SPCE device. This indicated the successful preparation of the cobalt nanosheet modified SPCE sensor device.

Fig. 5a shows the CV responses of the bare and cobalt oxide nanosheet (3–9 μL) modified SPCE UA sensors in a redox probe solution [(5 mM $[Fe(CN)_6]^{3-/4-}$ with 0.1 M KCl)] at a 50 mV s^{-1} scan rate. The 6 μL cobalt oxide nanosheet modified SPCE had a high CV current response, which further confirmed the efficient rate of charge transfer between the electrode surface and the probe solution (Fig. 5b). However, the 9 μL cobalt oxide nanosheet modified SPCE showed a decrease in current response. This was due to the increase in the film thickness, which resulted in the reduction of the electron transfer rate and a decrease in conductivity.[31,32]

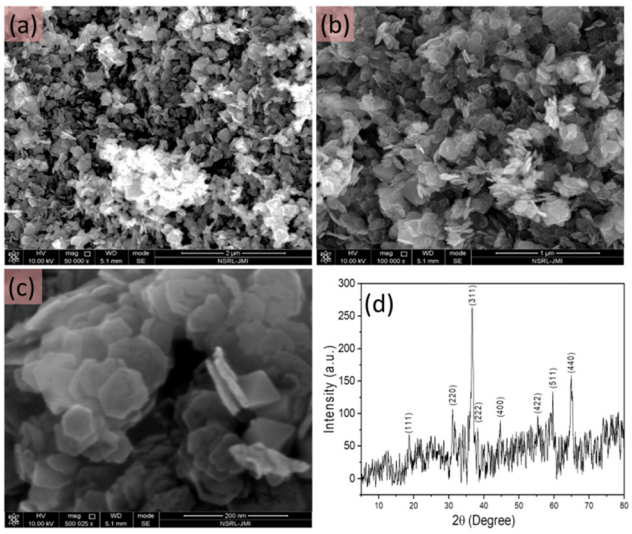

Fig. 2 FESEM images at different resolution (a–c) and the XRD pattern (d) of the as-synthesised hexagonal shaped cobalt oxide nanosheets.

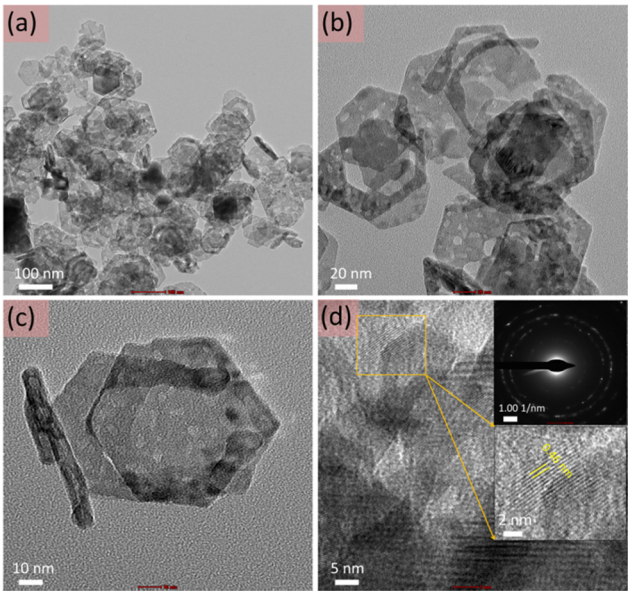

Fig. 3 The TEM images at different magnifications (a–c), and the HR-TEM (d) image of the hexagonal shaped cobalt oxide nanosheets. The insets in (d) are the SAED pattern (upper inset), and the magnified HR-TEM image (lower inset) of the hexagonal shaped cobalt oxide nanosheet.

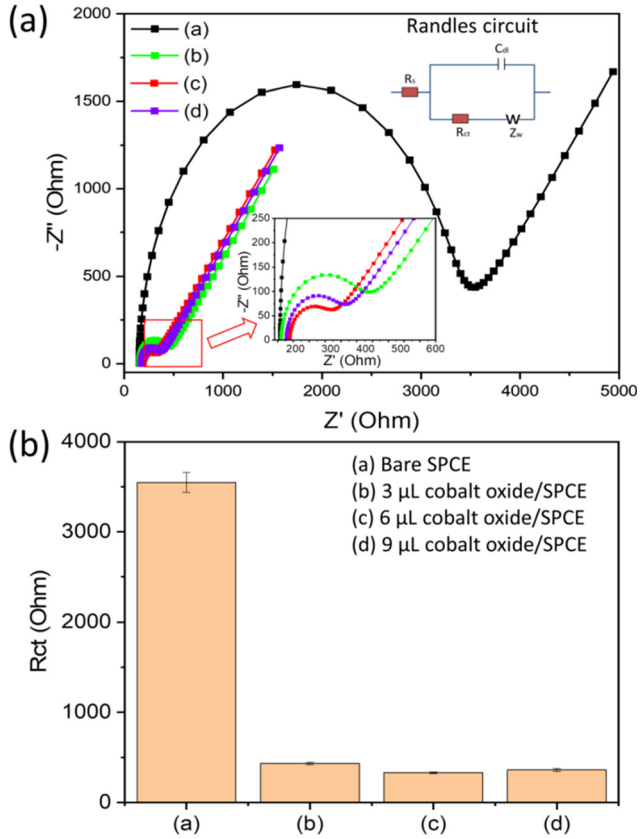

Fig. 4 The EIS Nyquist plots for sensor fabrication in 5 mM $[Fe(CN)_6]^{3-/4-}$ with a 0.1 M KCl probe solution. The EIS were obtained (a) using bare SPCE, (b) after fixing 3 µL cobalt oxide nanosheets on the SPCE, (c) after fixing 6 µL cobalt oxide nanosheets on the SPCE, and (d) after fixing 9 µL cobalt oxide nanosheets on the SPCE. Applied potential: +0.12 V. Frequency range: 0.1 Hz–100 kHz. (b) Histogram showing R_{CT} for the electrode (a–d) fitted using a Randles equivalent circuit (shown in the inset in (a)), where, Z_W is the Warburg resistor, R_{CT} is the charge transfer resistance, C_{dl} is the double layer capacitor, and R_S is the solution resistor.

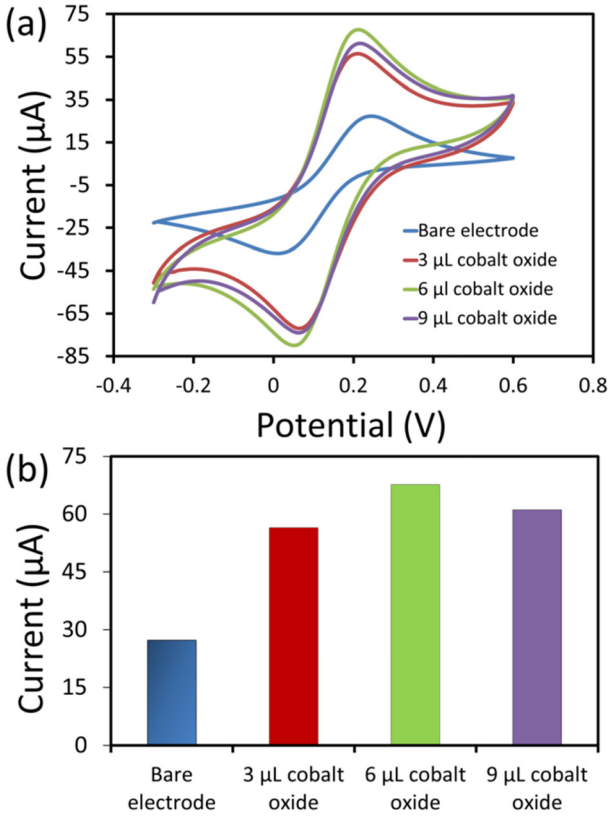

Fig. 5 (a) The CV responses of bare and cobalt oxide (3–9 µL) modified SPCE enzymeless UA sensors in 5 mM $[Fe(CN)_6]^{3-/4-}$ with a 0.1 M KCl redox probe solution (scan rate = 50 mV s^{-1}). (b) Histogram showing the peak current of bare and cobalt oxide nanosheet modified SPCE sensors.

Furthermore, the electrochemical performance of the 6 µL cobalt oxide nanosheets modified SPCE was examined in a redox probe solution (5 mM $[Fe(CN)_6]^{3-/4-}$ with 0.1 M KCl) at different scan rates (10–300 mV s^{-1}) (Fig. 6a). The CV current response significantly increased with the increasing scan rate. Fig. 6b displays the oxidation and reduction plot of the square root of the scan rate (mV $s^{-1})^{1/2}$ *vs.* redox peak current. The observed plot showed good linearity. There was a slight shift in the peak potential, which was due to the diffusion layer. The thickness of the diffusion layer was high at lower scan rates. Also, at the low scan rate, the alternating flux on the surface of the electrode became drastically low, and caused a shift in peak potential.

3.3. UA detection

The CV technique is highly sensitive and is commonly employed to investigate electron transfer initiated chemical reactions occurring in electrochemical sensors. Fig. 7a shows the CV response curves of the hexagonal cobalt oxide nanosheets/SPCE based enzymeless UA sensor in 100 mM PBS (pH = 7.4) without

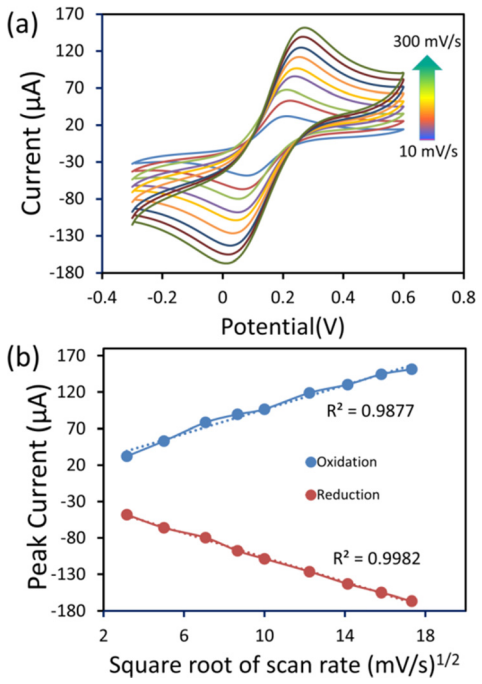

Fig. 6 (a) The CV responses of the best performing enzymeless sensor (6 µL cobalt oxide/SPCE) in a probe solution at different scan rates (10–300 mV s^{-1}), and (b) the oxidation and reduction plot of the square root of the scan rate (mV $s^{-1})^{1/2}$ *vs.* the redox peak current.

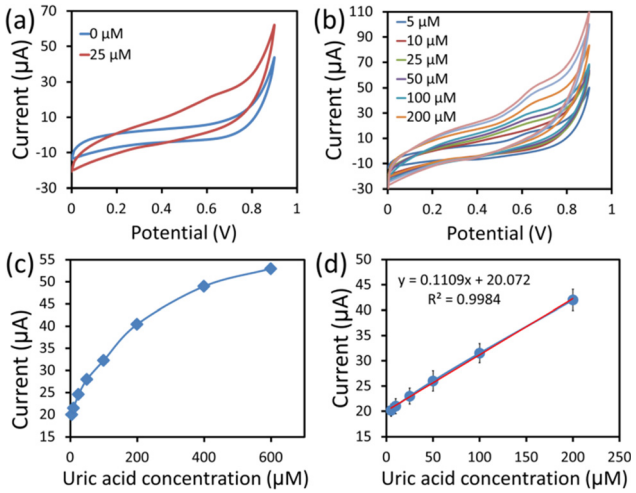

Fig. 7 (a) The CV response of the 6 μL cobalt oxide/SPCE sensor in the absence (0 μM) and presence (25 μM) of UA in PBS buffer at a 50 mV s^{-1} scan rate, (b) the CV response for different UA concentrations (5–400 μM) in PBS buffer at a 50 mV s^{-1} scan rate, (c) a plot showing oxidation current *vs.* UA concentration, and (d) calibrated linear range (5–200 μM) plot of the enzymeless sensor for three measurements.

UA (blue line), and with 25 μM of UA (red line) at 50 mV s^{-1} scan rates. It can be clearly seen from the response curves that the value of the current was increased in the presence of UA. The hexagonal cobalt oxide nanosheet modified SPCE UA sensor demonstrated the increase in the current value. This was due to the UA oxidation over the hexagonal cobalt oxide nanosheet surface that increased the electron mobility, and thus, the current response. The UA detection involved two electron transport phenomena, where the unique two-dimensional morphology of the hexagonal nanosheets provided large electrocatalytic active sites for UA oxidation.[29] In addition, it was also reported that the p-type nature of the cobalt oxide nanostructure provided excess holes (charge carriers) which resulted in the easy capture of electrons from the oxidation of UA.[33]

Next, the CV response curves were measured in various UA concentrations (5–400 μM) in PBS buffer at a 50 mV s^{-1} scan rate (Fig. 7b). When the UA concentration was simultaneously increased, there was a linear increase in the current value. Fig. 7c and d are the calibration plots of the anodic peak current *vs.* the UA concentration. The increase in the current response can be clearly seen with the increase in UA concentration from 5 to 400 μM, as shown in Fig. 7c. More detailed information was obtained from the calibration plot (peak current *vs.* UA concentration) of the linear range, shown in Fig. 7d. From the calibrated graph, the sensor responded linearly in the range of 5–200 μM UA concentration. A linear relationship ($y = 0.110x + 20.072$, $R^2 = 0.9984$) was obtained, where x and y are the current (μA) and UA concentration (μM), respectively. The sensitivity of the UA sensor was found to be 1560 μA mM^{-1} cm^{-2} using the equation (sensitivity = slope of the calibration curve/surface area). Also, the sensor showed a low LOD of ~5 μM), which was calculated based on an S/N ratio of 3. Overall, the constructed sensing platform exhibited ultra-sensitivity, a good linear range and LOD, which were comparatively better than those found in previous reports (Table 1).[8,9,18,19,34–40] This can be ascribed to the advanced sensing of UA using hexagonal cobalt oxide nanosheets.

3.4. Fabrication reproducibility, storage stability, and selectivity studies

To investigate the fabrication reproducibility, five similar hexagonal cobalt oxide nanosheet/SPCE UA sensors were fabricated following the uniform fabrication protocol (Fig. 8a and b). All the UA sensors showed an almost similar response with a relative standard deviation (RSD) of 4.3%, which showed the excellent reproducibility of the devices' fabrication under uniform conditions. The storage stability of the hexagonal cobalt oxide nanosheet/SPCE UA sensor was examined by repeating the measurements of 25 μM UA every week up to five weeks (Fig. 8c and d). The sensor was stored at room temperature (in dry conditions), when it was not in use. After five weeks

Table 1 Comparative sensing performance of our sensor with previous reports

Sensor electrode	Detection method	Sensitivity (μA mM^{-1} cm^{-2})	Linear range (μM)	Detection limit (μM)	Ref.
Cu_2O/ferrocene/uricase/GCE	DPV	1.9	0.1–1000	0.0596	8
NH_2-VMSF/ErGO/SPCE	DPV	—	0.5–180	0.129	9
Nanoflake-nanorod WS_2/GCE	DPV	312	5–1000	1.2	18
Co_3O_4 nanostructures/GCE	CV	—	500–3500	100	19
MoS_2/AlF	Amperometry	98.3	10–400	1.169	34
11-(Ferrocenyl)undecanethiol/Au	FET	—	0.1–1000	—	35
PAMTA/PG	DPV	131.98	5–1200	0.039	36
PPy-CB-Co_3O_4/GCE	CV	878.6	0.75–305	~0.46	37
$CuBi_2O_4$/FTO	CV	206.7	10–500	1.23	38
MWNTs/CILE	LSV	—	0.6–400	0.3	39
Co_3O_4 NPs/SPE	DPV	—	5–500	1.5	40
Co_3O_4 nanosheets/SPCE	CV	1560	5–200	~5	This work

Abbeviations: AlF: aluminium foil, Au: gold, CB: carbon black, CILE: carbon ionic liquid electrode, Co_3O_4: cobalt oxide, $CuBi_2O_4$: copper bismuth oxide, Cu_2O: cuprous oxide, CV: cyclic voltammetry, DPV: differential pulse voltammetry, ErGO: electrochemically reduced graphene oxide, FE: field effect transistor, FTO: fluorine-doped tin oxide, GCE: glassy carbon electrode, LSV: linear sweep voltammogram, MoS_2: molybdenum disulfide, MWNTs: multi-walled carbon nanotubes, PAMTA: poly-2-amino-5-mercapto-1,3,4-thiadiazole, PG: pencil graphite, PPy: polypyrrole, SPCEs: screen-printed carbon electrodes, SPE: screen-printed electrodes, VMSF: vertically-ordered mesoporous silica-nanochannel film, WS_2: tungsten disulfide.

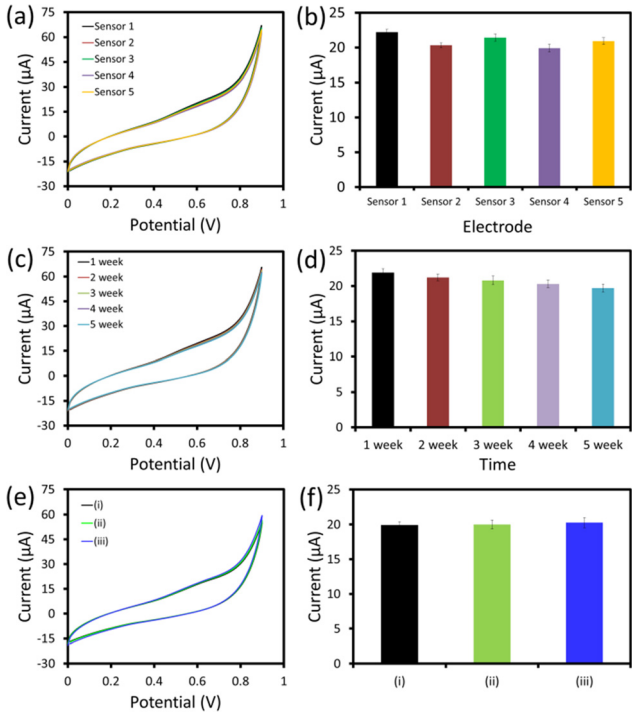

Fig. 8 (a and b) The CV response of the 6 μL cobalt oxide/SPCE sensor for 25 μM UA for five similar fabricated sensors, (c and d) the CV response of 6 μL cobalt oxide/SPCE sensor for 25 μM UA for up to five weeks, and (e and f) the CV response of sensor in the presence of 0 μM (i), 25 μM (ii), and 50 μM (iii) concentrations of each interferent with 25 μM UA.

of storage, the sensor retained almost 92.8% of the current response compared to its initial response measured after fabrication.

The selectivity of the fabricated sensor is a crucial parameter for the successful application of the sensor in real sample measurements. In order to determine the specificity and the selectivity of the fabricated sensor for UA, the sensing response to the interferents (L-cysteine, LA, K^+, Na^+ fructose, urea, and glucose) were tested after adding 25 μM (ii) and 50 μM (iii) concentrations of each of the interferents with 25 μM UA (Fig. 8e and f). The hexagonal cobalt oxide nanosheet/SPCE UA sensor showed an identical response with and without interferents. This showed there was no effect from the interferents on the sensing response of the sensor, further confirming the specificity of the sensor for UA with a strong anti-interference ability. The excellent fabrication reproducibility, storage stability, and selectivity confirmed that the sensor showed promise for use in future applications.

4. Conclusions

A simple strategy has been developed to synthesise hexagonal cobalt oxide nanosheets by a hydrothermal method. Hexagonal nanosheets like nanostructures were synthesised in a large quantity with a uniform morphology. The constructed sensor using hexagonal cobalt oxide nanosheets on the working electrode of SPCE showed an ultra-sensitive electrochemical response towards UA. In the presence of UA, the sensor showed an increase in their oxidation current. The cobalt oxide/SPCE UA sensor showed linearity up to 200 μM of UA with an ultra-sensitivity of 1560 μA mM^{-1} cm^{-2}. In addition, good stability, reproducibility, and specificity for UA were tested. The use of hexagonal cobalt oxide nanosheets greatly-increased the oxidation response, which showed that the as-synthesised nanostructure is suitable for use in the construction of highly sensitive sensors to detect other biomolecules.

Conflicts of interest

There are no conflicts to declare.

Acknowledgements

RA gratefully acknowledges the Ramalingaswami Fellowship Award and research funding grant (BT/RLF/Re-entry/28/2018) from the Department of Biotechnology (DBT), Government of India. MK and SM would like to thank the Ministry of Education, Government of India, for the Prime Minister's Research Fellows (PMRF) award.

References

1 M. Yazdani, A. Yazdani, K. Noori-Mahdavi, M. Kabiri, S. Baradaran and H. Nasri, *Shiraz E-Medical J.*, 2015, **15**, e26470.
2 S. Verma, J. Choudhary, K. P. Singh, P. Chandra and S. P. Singh, *Int. J. Biol. Macromol.*, 2019, **130**, 333.
3 X. Dai, X. Fang, C. Zhang, R. Xu and B. Xu, *J. Chromatogr. B: Anal. Technol. Biomed. Life Sci.*, 2007, **857**, 287.
4 Y. Guan, Q. Chu and J. Ye, *Anal. Bioanal. Chem.*, 2004, **380**, 913.
5 F. Y. Zhao, Z. H. Wang, H. Wang, R. Zhao and M. Y. Ding, *Chin. Chem. Lett.*, 2011, **22**, 342.
6 R. Ahmad, N. Tripathy, N. K. Jang, G. Khang and Y.-B. Hahn, *Sens. Actuators, B*, 2015, **206**, 146.
7 S. Zhao, J. Wang, F. Ye and Y.-M. Liu, *Anal. Biochem.*, 2008, **378**, 127.
8 Q. Yan, N. Zhi, L. Yang, G. Xu, Q. Feng, Q. Zhang and S. Sun, *Sci. Rep.*, 2020, **10**, 10607.
9 K. Ma, L. Yang, J. Liu and J. Liu, *Nanomaterials*, 2022, **12**, 1157.
10 Y. Wang, H. Xu, J. Zhang and G. Li, *Sensors*, 2008, **8**, 2043.
11 R. Ahmad, N. Tripathy, M.-S. Ahn and Y.-B. Hahn, *Sci. Rep.*, 2017, **7**, 46475.
12 S. Verma, J. Choudhary, K. P. Singh, P. Chandra and S. P. Singh, *Int. J. Biol. Macromol.*, 2019, **1**, 333.
13 R. Abdel-Karim, Y. Reda and A. Abdel-Fattah, *J. Electrochem. Soc.*, 2020, **167**, 037554.
14 R. Ahmad, O. S. Wolfbeis, Y.-B. Hahn, H. N. Alshareef, L. Torsi and K. N. Salama, *Mater. Today Commun.*, 2018, **17**, 289.
15 R. Ahmad, N. Tripathy, M.-S. Ahn, K. S. Bhat, T. Mahmoudi, Y. Wang, J.-Y. Yoo, D.-W. Kwon, H.-Y. Yang and Y.-B. Hahn, *Sci. Rep.*, 2017, **7**, 5715.

16 T. H. V. Kumar and A. K. Sundramoorthy, *J. Electrochem. Soc.*, 2018, **165**, B3006.
17 D. Hernández-Ramírez, L. H. Mendoza-Huizar, C. A. Galán-Vidal, G. Y. Aguilar-Lira and G. A. Álvarez-Romero, *J. Electrochem. Soc.*, 2021, **168**, 057522.
18 L. Durai, C. YiKong and S. Badhulika, *Mater. Sci. Eng., C*, 2020, **107**, 110217.
19 A. S. Chang, A. Tahira, F. Chang, N. N. Memon, A. Nafady, A. Kasry and Z. H. Ibupoto, *RSC Adv.*, 2021, **11**, 5156.
20 P. S. Gaikar, A. P. Angre, G. Wadhawa, P. V. Ledade, S. H. Mahmood and T. L. Lambat, *Curr. Res. Green Sustainable Chem.*, 2022, **5**, 100265.
21 X. Wang, A. Hu, C. Meng, C. Wu, S. Yang and X. Hong, *Molecules*, 2020, **25**, 269.
22 S. Ramesh, H. Yadav, C. Bathula, S. Shinde, A. Sivasamy, H.-S. Kim, H. S. Kim and J.-H. Kim, *J. Mater. Res. Technol.*, 2020, **9**, 11464.
23 D. Zhang, Q. Mi, D. Wang and T. Li, *Sens. Actuators, B*, 2021, **339**, 129923.
24 D. Zhang, C. Jiang, P. Li and Y. Sun, *ACS Appl. Mater. Interfaces*, 2017, **9**, 6462.
25 D. Zhang, Z. Yang, Z. Wu and G. Dong, *Sens. Actuators, B*, 2019, **283**, 42.
26 D. Zhang, H. Chang, C. Jiang, Y. Yao and Y. Zhang, *Sens. Actuators, B*, 2017, **252**, 624.
27 K. Białas, D. Moschou and F. M. P. Estrela, *Microchim. Acta*, 2022, **189**, 172.
28 P. Kannan, S. Boopathi, R. Kumaran, M. Kundu, M. Sasidhran and G. Maduraiveeran, *Mater. Res. Bull.*, 2019, **111**, 230.
29 V. Nagal, T. Tuba, V. Kumar, S. Alam, A. Ahmad, M. B. Alshammari, A. K. Hafiz and R. Ahmad, *New J. Chem.*, 2022, **46**, 12333.
30 Y. Zhang, M. Piao, H. Zhang, F. Zhang, J. Chu, X. Wang, H. Shi and C. Li, *J. Magn. Magn. Mater.*, 2019, **486**, 165272.
31 H.-M. Prasser, *Nucl. Eng. Des.*, 2021, **380**, 111304.
32 R. Porada, K. Jedlińska, J. Lipińska and B. Baś, *J. Electrochem. Soc.*, 2020, 167, 037536.
33 S. Masrat, V. Nagal, M. Khan, I. Moid, S. Alam, K. S. Bhat, A. Khosla and R. Ahmad, *Biosensors*, 2022, **12**, 1140.
34 R. Sha, N. Vishnu and S. Badhulika, *Sens. Actuators, B*, 2019, **279**, 53.
35 W. Guan, X. Duan and M. A. Reed, *Biosens. Bioelectron.*, 2014, **51**, 225.
36 R. G. Krishnan, R. Rejithamol and B. Saraswathyamma, *Microchem. J.*, 2020, **155**, 104745.
37 J. Ahmed, M. Faisal, S. A. Alsareii and F. A. Harraz, *Adv. Compos. Hybrid Mater.*, 2022, **5**, 920.
38 G. N. Sinha, P. Subramanyam, V. Sivaramakrishna and C. Subrahmanyam, *Inorg. Chem. Commun.*, 2021, **129**, 108627.
39 Y. Li, X. Zhai, H. Wang, X. Liu, L. Guo, X. Ji, L. Wang, H. Qiu and X. Liu, *Microchim. Acta*, 2015, **182**, 1877.
40 G. Turkkan, S. Zeki Bas, K. Atacan and M. Ozmen, *Anal. Methods*, 2022, **14**, 67.

